

Cyber Technology for Materials and Structures in Aeronautics and Aerospace

Final Report

R. Byron Pipes, PhD, NAE, IVA

September 30, 1999 to September 30, 2002

Department of Applied Science
College of William and Mary
Williamsburg, VA 23187

NASA Grant
NCC-1-356

- 1.0 Advanced Composites Development for Aerospace applications
- 2.0 Scale Effects in Carbon Nanostructures: Self-Similar Analysis
- 3.0 High temperature Polymeric Mesostructures and Foams

Advanced Composites Development for Aerospace Applications

Darrel Tenney¹, PhD and R. Byron Pipes², PhD, NAE

1: Aerospace Vehicle Systems Technology Program Office, NASA Langley Research Center
E-mail: d.r.tenney@larc.nasa.gov

2: 17th President, Rensselaer Polytechnic Institute
E-mail: rbpipes@wm.edu

Abstract

The evolution of composites applications in aeronautics from 1970 to the present is discussed. The barriers and challenges to economic application and to certification are presented and recommendations for accelerated development are outlined. The potential benefits of emerging technologies to aeronautics and their foundation in composite materials are described and the resulting benefits in vehicle take off gross weight are quantified. Finally, a 21st century vision for aeronautics in which human mobility is increased by an order of magnitude is articulated.

Keywords: Advanced composites, Aeronautics, 21st century vision

Introduction

Advanced composites have emerged as the structural materials of choice for many aerospace applications because of their superior specific strength and stiffness properties. First developed for military aircraft applications, composites now play a significant role in a broad range of current generation military aerospace systems. Commercial transport aviation has also witnessed a significant increase in adoption

of composites during the past ten years. And there are currently a large number of general aviation aircraft with significant use of composite materials and structures that anticipate FAA flight certification in the near future.

Yet, there continue to be barriers and challenges to the expanded exploitation of composites technology for primary transport aircraft structures, i.e. wing and fuselage. These include damage tolerance, fuel containment, lightning protection, repair and nondestructive inspection, modeling and failure prediction and cost effective manufacturing. The successful resolution of these issues requires additional research directed at the underlying science through comprehensive programs of research and development. Development of standard engineering practices for exploitation of contemporary composites technology for near term applications can also be expected to benefit new aerospace products under current development.

The future composites technology will provide the platform for the next revolution in aerospace vehicle technology. With recent advances in science and engineering there are new emerging technologies that will likely accelerate the development of aerospace

vehicle design during the next decade including: sensors and devices, intelligent materials and structures, active flow control, reliability-based design and certification, robust manufacturing technology, nanotechnology and biomimetics. Moreover, it is the strategic integration of these technologies that will provide for the next major gains in vehicle performance. Yet the integration of these technologies cannot be achieved with contemporary materials and structures technologies. Therefore, it is essential that significant effort be directed to develop the next generation composites technology.

Current Status

The applications of composite materials in aerospace products are pervasive today, having found their first applications in military aircraft in the early 1970's. The evolution of this important technology has been multifaceted with the initial phase led by the defense industry, significant advances in the commercial aircraft and rotorcraft industries and its most aggressive exploitation in the general aviation industry. Advanced composites can trace its origin to the invention of the boron filament in the United States and the carbon fiber in Japan/United Kingdom in the 1960's. The first production aerospace application was the horizontal stabilizer of the U.S. Navy F-14 in 1970, followed shortly thereafter by applications in the U.S. Air Force F-15 and F-16. During the decade of the 1980's commercial applications were initiated through the NASA ACEE Program. The Boeing 737 horizontal stabilizer was certified in 1982 and applications with composites approaching 10 wt.% were achieved with the Airbus 300 and 310, Boeing 737, 757 and 767, McDonnell-Douglas MD-82, 83 and 87 during the 1980's. The Airbus 320 was first commercial aircraft to exceed the 10% utilization. By 2000, applications approaching 30% weight savings had been

achieved by the U.S. Air Force B2 and F-22 and the U.S. Navy V-22. The industry is now poised to develop commercial and military airframes with extensive composite wing, empennage and fuselage applications. The Boeing "Sonic Cruiser" and the 650-seat A380 Airbus will likely be the next examples of the use of composites in future commercial aircraft. Two new business jets with composite sandwich designs in pressurized fuselage have been recently undergone consideration for certification by the FAA. The Raytheon Premier I has been flight certified and the AASI Jetcruzer 500 is well into the process. Propeller-driven aircraft have also incorporated composite materials in their airframes. The PAC USA Lancair LC40-550FG and the Cirrus Design Corp. SR 20 were type certified in 1998 [1]. New rotorcraft vehicles include composites applications in airframe, rotor blades and rotor drive systems (main and tail). The Sikorsky S92 rotorcraft and the Bell Textron BA609 Tiltrotor are two such examples.

Barriers and Challenges: Economics and Certification

Barriers to expanded application to composite materials in aircraft are shared by the defense, commercial and general aviation industries. Manufacturing and non-recurring development costs continue to limit the rate of growth of the field. Current engineering practice is a test-based, building-block approach that is test intensive. Empirical design and process standardization and maintenance technology are also issues of concern. The lack of standardization of material forms and high fidelity, hierarchical design methodologies can result in overly conservative designs that, while providing performance gains and ensuring safety and durability, too often suffer in economy compared to conventional metals technology. Validated progressive failure analyses are also required to predict, without tests, the lifetime performance of composite structures.

Finally, the limited human resources with composites training and experience constrain broader applications [1].

It is also important to point out recent advances that are paving the way to meeting the challenges articulated above. NASA Langley recently successfully tested a full-scale composite wing structure (see Fig. 1) designed to meet the requirements of a 220-passenger commercial transport aircraft [2]. The wing box was 41 feet in length and incorporated advanced graphite fiber textile performs and Kevlar stitching for stringer-skin connections with resin-film-infusion to achieve resin impregnation. These manufacturing innovations by the Boeing Company were focused upon significant manufacturing cost reductions while meeting performance goals. The wing structure sustained 97% of design ultimate load prior to failure through a lower access opening and was, therefore, judged to have successfully met test requirements while providing further insight into refinements necessary for adoption of this new technology.

It should also be noted that the successful design and test of the NASA/Boeing wing structure required an extensive set of material, fabrication and sub-element tests to clarify manufacturability and the preliminary design. Thus, at the end of the 20th century composites technology is found to be largely based in empirical methods with the accompanying limits on economy (See Figure 2). These shortcomings in composites technology will only be overcome with the further developments in the areas described and through new emerging technologies.

Emerging Technologies

There are a number of emerging technologies that will expand the design space in the 21st century air vehicle and provide enhancements in performance, safety and economy. Smart materials and systems

technology to control structural and aeroelastic response offer the opportunity to achieve structural and aeroelastic performance and efficiencies not possible with conventional materials and structures technology. Enhanced flutter, gust, buffet and maneuver load behavior can be achieved. Piezoelectric actuators have been successfully employed for active flutter suppression, active gust load alleviation and noise suppression [3]. Shape memory alloys have also been employed to address sonic fatigue and noise suppression issues. Smart structures have been developed to improve aerodynamic performance in such applications as the contoured, hingless flap and aileron with built-in shape memory alloy tendons. Efficiency gains of 8-12% have been achieved for lift, pitching and rolling moments over a broad range in wind tunnel tests [4]. The engine inlet has also been the subject of smart structures development in order to provide for its deformation to achieve optimum configurations for multiple flight conditions.

Synthetic jet actuators for control of flow separation have recently been employed to increase airfoil efficiency. The actuator has the capacity to provide both positive and negative pressure in the flow stream at a small diameter orifice and is thereby termed a "zero-mass flow" device [5]. Jets constructed of two piezoelectric/metal wafer laminates that are actuated by controlling sinusoidal frequency and phase to achieve the desired pressure characteristics. Jet velocities of 60-100 m/second have been achieved in the laboratory and active separation control at Reynold's number up to 40X106 has been demonstrated to delay flow separation under flight conditions [6].

Multidisciplinary design optimization and flight control disciplines have been integrated to utilize localized flow control and distributed shape-change devices to achieve active flight control for tail-less aircraft. The

integration of vehicle configuration, prediction of control moments with computational fluid dynamics, location of shape-change devices, and algorithm for optimum location of devices and simulation of the flight controls, was necessary. In addition, fluidic thrust vectoring, accomplished by deflection of the jet with a secondary air stream, has been examined for additional flight control [7].

Reliability-based design and certification require that new and robust methodologies be developed for high fidelity analysis of composite materials and structures [8]. This approach will replace the empirically based, factor-of-safety design with a design paradigm that features science-based methodology for critical design features. It relates weight, reliability and economics as multiple design merit functions. Process specific imperfections and defects and their impacts on response are considered directly. Progressive failure analyses are carried out with powerful design tools made possible by the integration of advanced modeling methods and scientific understanding. Finally, tailored composite applications based upon biologically inspired concepts to achieve optimum performance are being pursued.

Robust manufacturing technology to insure high performance aerostructures with increased cost-effectiveness has focused on the development of non-prepreg/autoclave systems. The integration of engineered textile preforms, stitching and vacuum-assisted resin transfer molding technology has been shown to provide significant advantages for future aircraft programs. Methods for prediction of manufactured quality, reproducibility and imperfections will be essential.

The field of biological sciences continues to provide new insights into the ways organisms have successfully adapted to their

environment over millennia. The integration of materials, structures and aerodynamics simulations with the field of biomimetics provides the framework to develop a link between what nature has learned over time and the need for current aerospace solutions. These efforts require the development of design teams who have representation from the disciplines of biomimetics, materials science, aerostructures, computational fluid dynamics and computer science.

Nanotechnology can also be expected to provide the next generation of revolutionary materials technology for future aero vehicles. Discovered by Iijima [9] the single-walled carbon nanotube possesses extraordinary mechanical, electrical and thermal properties. Early evidence suggests that carbon nanotube/polymer composites will play a significant role in the future aero vehicle systems.

Technology Integration Benefits

The future of aeronautics will significantly benefit from the integration of the numerous advances discussed above and their exploitation will be based in advanced composites as the enabling technology [10]. For military aircraft, smart, flexible structures, synthetic jets, forebody vortex control, advanced control laws, passive porosity, continuous moldline technology and fluidic thrust vectoring will provide for increases in range, improvements in agility and survivability. For commercial transport vehicles, these technologies will provide active shape control, health monitoring, buffet load alleviation, active transition control, thrust vectoring, inlet and nozzle shaping, exterior noise suppression, vibration suppression, active separation control, gust load alleviation and flutter suppression.

Consider the contributions of these technologies for a conventional long haul/high capacity conventional subsonic

transport aircraft. Laminar flow control, design optimization and excrescence drag reduction will yield a reduction of 4.6% in the take off gross weight (TOGW) of the vehicle [11]. Composite wing and tails, composite fuselage, light weight landing gear, advanced metals and aeroelastic tailoring will reduce TOGW by 24.3%. Advances in aero-mechanical propulsion design, hot section, materials and secondary systems can achieve a savings of 13.1%. Finally, in the systems area, relaxed static stability, fly-by-light/power-by-wire, high performance navigation and intelligent flight systems will yield a 9% savings in TOGW. Taken together these advances would yield an aircraft with an overall weight reduction of 51%. Of the total weight reduction, structures technology and composites would account for 48% of the total.

The blended wing body concept to produce a long haul/high capacity subsonic transport aircraft with a capacity of 800 passengers, a range of 8500 nautical miles and a landing requirement of 10,000 feet could achieve a 45.7% weight savings (TOGW) through the incorporation of advanced technology. Laminar flow control, design optimization, and excrescence drag reduction would yield 11.8% savings. Composite wing and fuselage, light weight landing gear and aeroelastic tailoring would reduce weight by 19.1%. In the propulsion arena advances in aero-mechanical design, hot section, materials, secondary systems, boundary layer ingestion would yield 12.2% and in the systems area, fly-by-light/power-by-wire, high performance navigation and intelligent flight systems would reduce weight by 2.6%. Clearly, the technology with the greatest impact on weight remains structures technology and composites for the blended wing body concept vehicle as well as the conventional concept discussed above.

21st Century Vision for Aeronautics Technology

Technology in the Digital Age will revolutionize high-speed mobility of humankind in a manner that will produce a sea change in human prosperity. This change will be not unlike the completion of the intercontinental railroad in the late 1800's or the introduction of the interstate highway system in the 1950's in the United States. Today's air mobility of citizens is limited by analog air traffic control systems, the number of trained pilots, the number of full-scale airports and the number and character of aircraft. Future Digital Airspace technology will provide the vehicle with "perfect knowledge" of terrain, geography, weather, vehicle condition, control and navigation through the central digital brain with extraordinary computational power. Embedded sensors and devices will yield smart materials and structures sufficient to achieve performance that allows vehicles to significantly increase performance and land safely on airfields that are insufficient in length for conventional aircraft. This revolution in technology will increase human mobility by an order of magnitude (See Figure 3). However, it is clear that the integration of the necessary technologies will lead to increased complexity of the air transportation system as well as air vehicles. Indeed, as the enhanced capability of the "digital machine" is increased, there will be a significant increase in system complexity such that the technology insertion will appear disruptive. During the next phase, however, increases in capability will result in only a corresponding linear increase in system complexity. It is during this period of technology innovation that the primary benefits described above will be realized.

The primary question to be answered is, "will the benefits in mobility, performance, safety, noise reduction, fuel economy be worth the price required to master complexity of the

multifunctional vehicle and the “open space” air traffic control systems?” One need only examine the benefits of the digital processor in today’s society, as described in Moore’s Law to answer, yes! Computational power has doubled every eighteen months during the last several decades and it was the mastery of the complexity of modern microelectronics that is responsible for the extraordinary economic growth in much of the world today. Enhanced high-speed air mobility can be expected to produce no less result.

References

1. Ilcewicz, L. and Cheng, L., “Draft Memorandum for National Plan on Safety and Certification Initiatives for Composites Used in Aircraft Products,” (2001).
2. Jegley, D.C. and Bush, H.G., AIAA Paper No. 2001-1334-CP, (2001).
3. McGowan, A.R., et al, 5th SPIE International Symposium on Smart Structures and Materials: Industrial and Commercial Applications, Paper 3326-21, San Diego, CA, March (1998).
4. Kudva, J.N., et al, 8th SPIE Annual Symposium: Industrial and Commercial Applications, Paper 4332-48, Newport Beach, CA, March (2001).
5. Chen, F.-J., et al, AIAA Paper 2000-2405, (2000).
6. Seifert, A. and Pack, L., AIAA Paper 2000-2542, (2000).
7. Deere, K.A., AIAA 2000-3598, (2000).
8. Hilburger, M.W. and Starnes, J.H., AIAA-2001-1394, (2001).
9. Iijima, S., Nature, 354, (1991), 56.
10. Tenney, D.R. and Hernandez, G., 21st Congress of the International Council of Aeronautical Sciences, Melbourne, Australia, (1998).
11. McKinley, R.E., “Blended-Wing-Body: Design Challenges for the 21st Century,” 2nd Internat. Conf. On Nonlinear Problems in Aviation and Aerospace, April (1998).

Figures

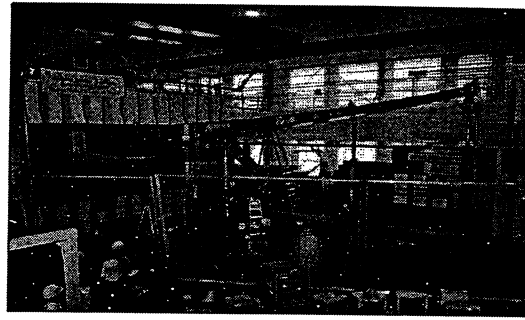


Fig. 1 Boeing – Langley composite wing test

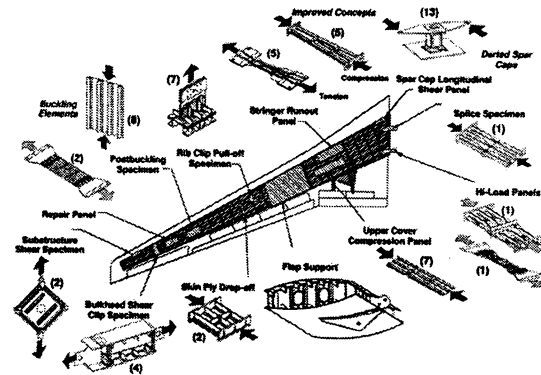


Fig. 2 Building block approach

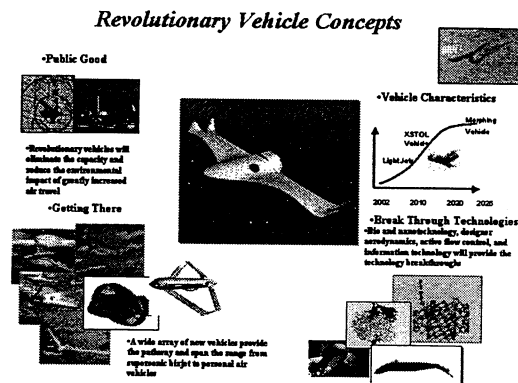


Fig. 3 Revolutionary vehicle concepts.

SCALE EFFECTS IN CARBON NANOSTRUTURES: SELF-SIMILAR ANALYSIS

R. Byron Pipes
The University of Akron, Akron, OH, USA

Pascal Hubert
Old Dominion University, Norfolk, VA, USA

Abstract

The present study focuses on the creation of a framework and methodology to span three orders of magnitude in scale with interconnected models that relate performance of single wall carbon nanotubes (SWCN) at the nanometer scale to a *nano-array*, *nano-wire* and *micro-fiber* with self-similar geometries. The geometry chosen is the helical array, where at the nanoscale, the properties of nanotube crystals (collimated arrays) predicted by the method of lattice dynamics are employed to predict properties of the elements in helical nanotube array. The properties of the *nano-array* of circular cross section are then predicted through a layered cylinder analysis in anisotropic elasticity. The *nano-array* properties are then used to describe the properties of elements in a second helical array, the *nano-wire* consisting of the helical arrays suspended in a polymeric matrix. Next the *nano-wires* are assembled in a third helical array composite to form the *micro-fiber*. The three-step analysis involves models that are identical in geometry, except that they differ in scale and are thereby, self-similar. For a single walled nanotube of diameter of 1.38×10^{-9} meters, the resulting *nano-array* diameter is 1.48×10^{-8} meters (equilibrium packing fraction of 79%), the *nano-wire* diameter is 1.69×10^{-7} meters (packing

fraction of 70%) and the *micro-fiber* diameter is 1.32×10^{-6} . Perhaps the most interesting aspect of the study is the focus on translation of properties from the nanoscale to the microscale and the scale transfer efficiencies. The present study presents predictions for the mechanical properties of the helical *nano-array*, the *nano-wire* and the *micro-fiber* such as the axial Young's modulus, shearing modulus and Poisson's ratio.

Keywords: nanotube, nanofiber, scaling, self-similar, elastic properties.

1. Introduction

The discovery of single walled carbon nanotube (SWCN) has lead to numerous studies that predict the development of high performance materials with extraordinary mechanical properties [1]. Yet there remains the challenge to develop compositions and material structures at the nanoscale that can be scaled into materials at the macroscale. A recently published image of a nanotube array appeared in Science [2] (Fig. 1) showing what appears to be a hexagonal packing of collimated carbon nanotubes. With the knowledge that conventional nanotubes are of finite length, this investigation focuses on the potential for assembling large numbers of

carbon nanotubes in collimated arrays wherein the nanotube properties are translated from the nano to the micro scale. The element of helicity is introduced as it is in textile fiber yarns to enhance load transfer between the discontinuous nanotubes. The prediction of the elastic properties of a helical array of collimated reinforcing elements is described in an earlier paper by the authors [3].

2. Self-similar approach

A three-step process is described in the present work wherein discontinuous SWNC are assembled into a *micro-fiber* as illustrated in Fig. 2 and summarized in Table 1. In the first step, a helical array of diameter 1.48×10^{-8} m, made up of SWCN, of outside diameter (D_o) 1.38×10^{-9} m, inside diameter (D_i) 0.73×10^{-9} m and average length 4.8×10^{-7} m, is assembled so that the nanotube center-to-center spacing (s) is 1.48×10^{-9} m. The SWCN spacing corresponds to a volume fraction of 0.79 was determined from the SWCN array image shown in Fig. 1 and a representative hexagonal image is illustrated in Fig. 3.

The first array is termed the SWCN *nano-array* where ninety-one SWCN make up the cross-section of the helical *nano-array* and the helical angle (α) is 10 degrees. The continuous SWCN *nano-arrays* are next surrounded by a polymeric matrix with a volume fraction (V_f) of 0.70 and assembled into a second twisted array of diameter 1.69×10^{-7} m, termed the SWCN *nano-wire*. Finally, the SWCN *nano-wires* are impregnated with a polymer matrix and assembled into the final helical array – the SWCN *micro-fiber* of diameter 1.93×10^{-6} m. It is important to note that the geometries of the three arrays are self-similar and the same analytical model is utilized for prediction of the mechanical properties of each array as will be discussed in the following. Fig. 3 illustrates the assembly of the three arrays into the *micro-fiber*. It is noteworthy that for the configuration described, approximately 1.6

trillion SWCN are required to produce a length of *micro-fiber* equal to one meter.

Scale	Diameter (m)	Matrix	V_f
SWCN	1.38×10^{-9}	-	-
nano-array	1.48×10^{-8}	none	0.79
nano-wire	1.69×10^{-7}	polymer	0.70
micro-fiber	1.93×10^{-6}	polymer	0.70

Table 1: Scale input parameters.

3. Helical array and micromechanics analyses

The layered cylinder analysis replaces each of the three arrays with a layered cylinder with effective layer properties and with tangent of the helical angle varying linearly with radial position in order to represent twist in the array. The helical angle of each layer is distinct and is determined by its radial position from the cylinder axis. For the *nano-array*, it is assumed that the discontinuous nanotubes are collimated, lay within the cylindrical layer surface. The volume fraction of carbon nanotube is taken as 0.79 (Fig. 3).

The layer properties of the *nano-array* crystal (Table 2) were obtained from the work of Popov et al. [4] and from estimates by the authors and are consistent with Ref. [5]. E_L , E_T and ν_{LT} were obtained for a crystal composed of SWCN with a diameter of 1 nm [4]. Values for G_{LT} , G_{NT} and ν_{NT} were assumed by the authors. A value of 894 GPa was taken as the Young's modulus of SWCN [6].

The cylinder analysis focuses on the behavior of a layered cylinder with helical anisotropy (Fig. 4). The concentric layers are assumed to be perfectly bonded together. Continuity of radial stress and radial displacement at the layer interfaces is assured. Finally, the cylinder is subjected to combination of uniform extensional

strain, w_0 (m/m), torsional shearing strain/radius, v_0 (rad./m), torque, T (N-m), and axial force, F (N).

E_L^*	650 [GPa]
E_T^*	16.1 [GPa]
G_{LT}^{**}	5.80 [GPa]
G_{NT}^{**}	5.80 [GPa]
ν_{LT}^*	0.16
ν_{NT}^{**}	0.40

* From Popov. et al. [4]

** Assumed by authors.

Table 2: *Nanotube array properties.*

For the *nano-wire* and *micro-fiber*, the elastic properties of each layer of the multi-layered cylinder are determined by using micromechanics relations from Bogetti and Gillespie [7].

4. Self-similar property results

The results for Young's modulus, shearing modulus and Poisson's ratio are presented in Fig. 5-7 for the four geometries and scales investigated: SWCN (10^{-9}), *nano-array* (10^{-8}), *nano-wire* (10^{-7}), and *micro-fiber* (10^{-6}). As such, these results illustrate the translation of properties from the nanoscale to the microscale for the self-similar helical array geometry. It is noteworthy that the modulus of the *nano-array* is less than 30% of the nanotube, while the Poisson's ratio of the array is seen to increase from 0.23 to 0.47. The latter property is strongly influenced by the 10 degree twist of the array. As the *nano-array* elements are assembled to produce the *nano-wire*, there is a continued reduction in modulus and increase in Poisson's ratio, but at a diminished rate compared to the *nano-array*. Finally, the properties of the *micro-fiber* are shown to differ significantly from those of the SWCN. Young's modulus is diminished by approximately 68% in moving from the nano to the micro

scale. Indeed, the predicted modulus of the *micro-fiber* is seen to be less than that of a conventional, intermediate modulus carbon fiber.

The normalized modulus (array modulus/SWCN modulus) predictions for the three array geometries are presented in Fig. 8. The primary influence upon modulus reduction of the *nano-array* compared to the SWCN is the packing fraction of 0.79 yields an effective 21% reduction, while the load transfer efficiency and helical geometry produces a reduction of 9%. These effects are cumulative and acting together they yield a 30% decline in modulus of the *nano-array* compared to the SWCN.

Taking the helical *nano-array* as the reinforcing element in the *nano-wire* yields an array consisting of continuous reinforcing elements with load transfer efficiency of 1.00 and a packing fraction of 0.70. While the maximum packing fraction in a hexagonal geometry is 0.92, the 0.70 fraction was chosen as a practical upper bound. The reinforcing elements were assumed to be surrounded by a polymeric matrix material. Moving from the *nano-array* to the *nano-wire* resulted in a 31% reduction in normalized modulus, corresponding closely to the influence of reinforcing volume fraction.

Finally, the reduction in normalized modulus of the *micro-fiber* (Fig. 8) compared to its reinforcing element, the *nano-wire*, appears to reflect primarily the influence of packing fraction. Indeed, the effective packing fraction of SWCN in the *micro-fiber* is the product of the three packing fractions or 0.39. The resulting efficiency ratio for the *micro-fiber* is 0.32.

The density of the array geometries (Fig. 9) is important in determining the specific modulus (modulus/density) of the *micro-fiber*. The primary parameter responsible for reduction in array density is the volume fraction of the reinforcing element

and the density of the matrix phase. The density of the SWCN is taken to be 1.33 g/cm^3 . For the *nano-array*, the packing fraction of the SWCN determines the effective density, which was determined to be 1.05 g/cm^3 . The polymer matrix density is taken as 1.0 g/cm^3 . Only modest changes in density occur for the *nano-wire* and *micro-fiber* since the density of the matrix polymer and the *nano-array* differ only slightly.

Combining the results illustrated in Fig. 5 and 9 allows for the determination of the specific moduli of the three array elements as shown in Fig. 10. Here the results decline from 595 GPa for the SWCN to 595 for the *nano-array* to 408 for the *nano-wire* to 279 for the *micro-fiber*. Specific moduli for all three arrays are seen to exceed that of the conventional carbon fiber of 155. When these results are normalized with respect to the carbon fiber specific modulus, the trend presented in Fig. 11 results. From a ratio of specific modulus of the SWCN to conventional carbon fiber of 4.3, the specific modulus of the *micro-fiber* is shown to be 1.8 times that of the carbon fiber.

5. Conclusions

The present study has focused on the creation of a framework and methodology that spans three orders of magnitude in scale with interconnected models to relate the Young's modulus of the SWCN at the nanometer scale to a *micro-fiber* three orders of magnitude larger in diameter. The interactions between collimated and twisted nanotubes within the *nano-array* were represented by nanotube crystal properties predicted by lattice dynamics and mapped into layer properties of a helical cylinder to represent the twisted array. The properties of three arrays, *nano-array*, *nano-wire* and *micro-fiber*, were then predicted through a layered cylinder analysis in anisotropic elasticity. The *nano-array* properties were used to describe the properties of helical reinforcing elements in the

nano-wire and its Young's modulus was predicted. *Nano-wires* were then assembled into a third helical array to predict the modulus of the *micro-fiber*. This three-step analysis for the prediction of Young's modulus of the *micro-fiber* involved models identical in geometry, but different in scale and were thereby, self-similar. For a single walled nanotube of diameter of 1.38×10^{-9} meters, the resulting *nano-array* diameter was 1.48×10^{-8} meters (equilibrium packing fraction of 79%), the *nano-wire* diameter was 1.69×10^{-7} meters (packing fraction of 70%) and the *micro-fiber* diameter was 1.93×10^{-6} .

The translation of specific Young's modulus from the nanoscale to the micro-scale and the scale transfer efficiencies have been presented and analyzed to reveal an overall reduction of 78%. Of the individual influences of load transfer efficiency, matrix properties, packing geometry and the latter is seen to be dominant. Finally, the success in developing a framework for the determination of the translation of properties of the SWCN to structural elements at the micro scale has been demonstrated. More research is required to further clarify the application of lattice dynamics methods in predicting SWCN array properties. Further, the assumption of a constant load transfer efficiency at all scales is approximate.

The results presented in the present work focus on the stiffness properties of the multi-array geometries. Strength translation of the SWCN to the *micro-fiber* consisting of the microstructural geometries described in the present work is unlikely to follow similar trends as the modulus since strength is likely to be controlled by local phenomena while stiffness is an average property for a heterogeneous body. It is possible that the extraordinary strength properties of the SWCN can be sustained at the microscale.

6. References

- [1] Iijima, S., (1991), *Nature*, **354**, pp. 56.
- [2] Thess, A., Lee, R., Nikolaev, P., Dai, H., Petit, P., Robert, J., Xu, C., Lee, Y. H., Kim, S. G., Rinzler, A. G., Colbert, D. T., Scuseria, G., Tománek, D., Fischer, J. E., Smalley, R. E., (1996), *Science*, **273**, pp. 483.
- [3] Pipes R. B., Hubert, P., (2001), *Composites Science and Technology*, in press.
- [4] Popov, V. N., Van Doren, V. E., Balkanski, M., (2000), *Solid State Communications*, **114**, pp. 395.
- [5] Popov, V. N., Van Doren, V. E., (2000), *Physical Review B*, **61**, 4, pp. 3078.
- [6] Salvenat, J-P., Briggs, G. A. D., Bonard, J-M., Bacsá, R. R., Kulik, A. J., Stöckli, T., Burnham, N., Forro, L., (1999), *Physical Review Letters*, **82**, 5, pp. 944.
- [7] Bogetti T.A., Gillespie, J.W., (1992), *Journal of Composite Materials*, **26**, pp. 5626.

6. Figures

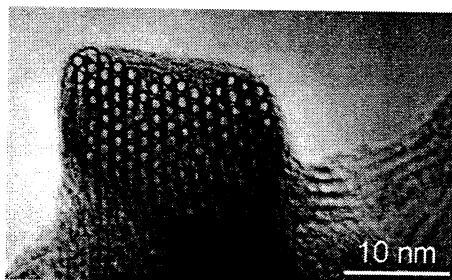


Figure 1: SWCN rope from [2].

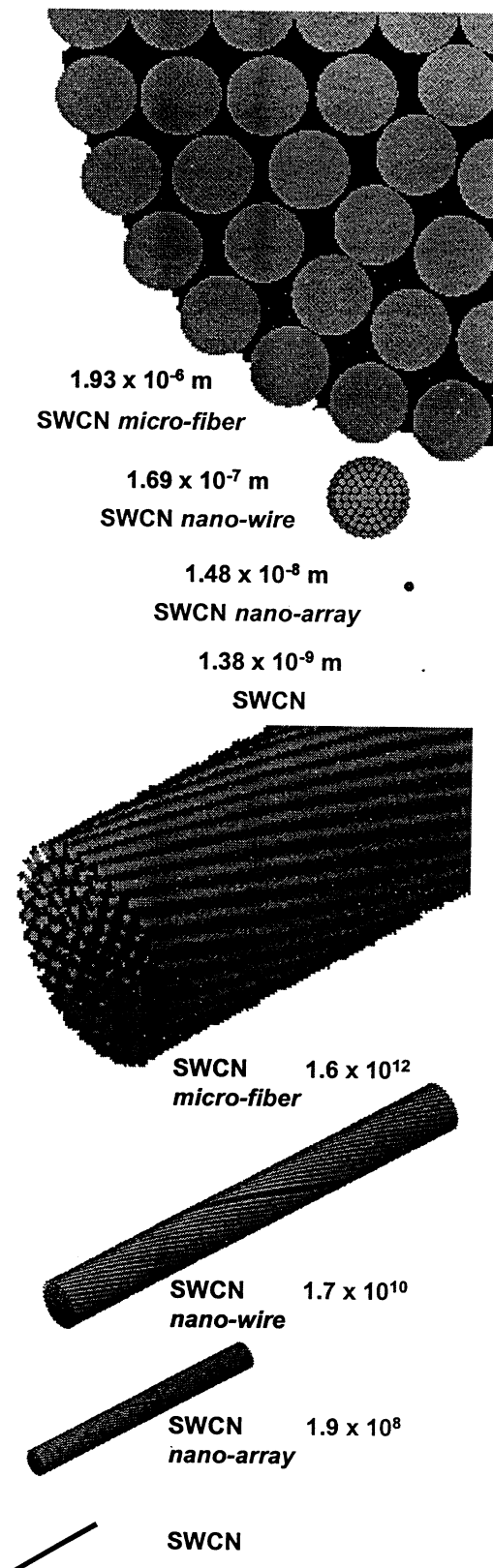


Figure 2: a) Self-similar scales and b) number of SWCN per meter length.

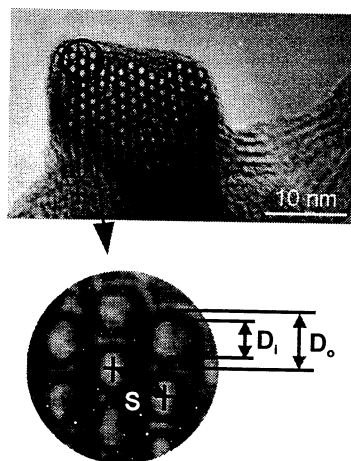


Figure 3: Array image analysis.

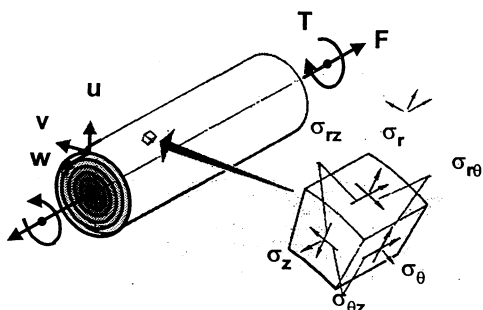


Figure 4: Concentric cylinder nomenclature.

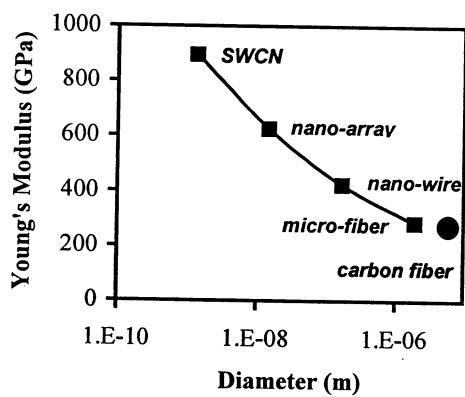


Figure 5: Young's modulus.

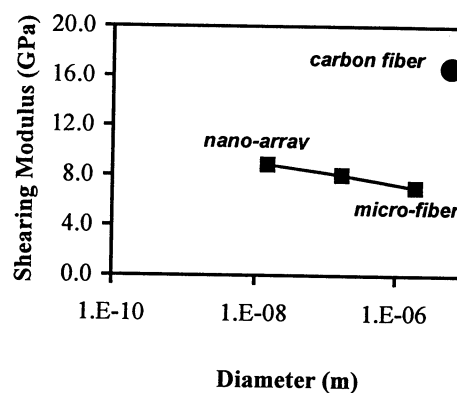


Figure 6: Shearing modulus.

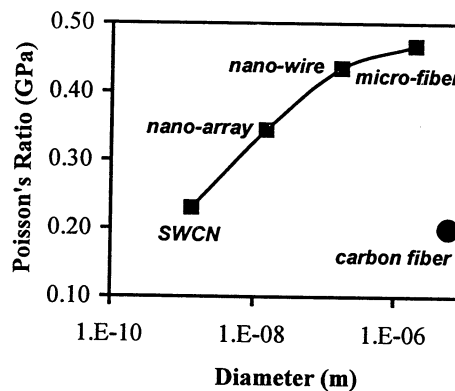


Figure 7: Poisson's ratio.

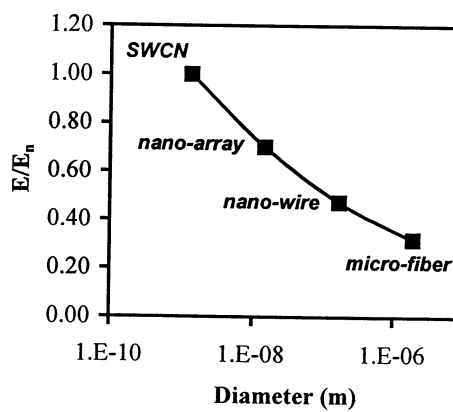


Figure 8: Normalized Young's Modulus (E/E_n).

Figure 11: *Normalized specific modulus, $(\text{specific modulus})_{\text{array}}/(\text{specific modulus})_{\text{carbon fiber}}$.*

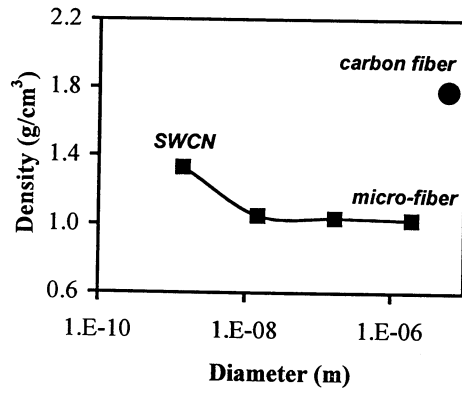


Figure 9: *Density.*

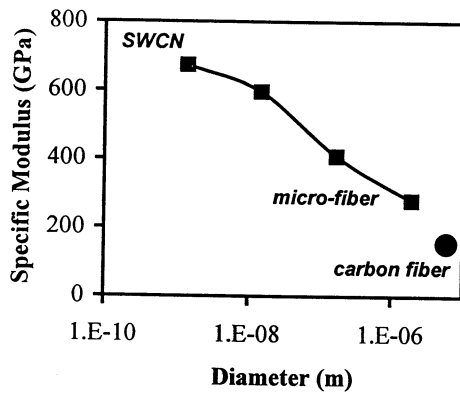
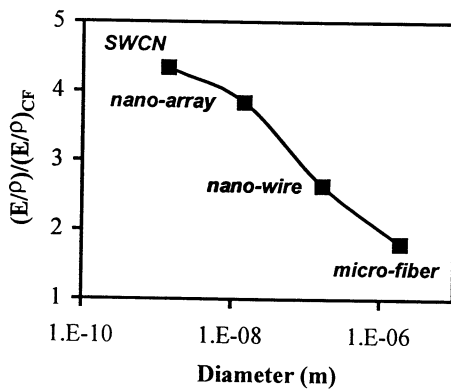


Figure 10: *Specific modulus.*



HIGH TEMPERATURE POLYMERIC MESOSTRUCTURES AND FOAMS

R. Byron Pipes
The University of Akron, Akron, OH, USA

B. Gonsoulin
Old Dominion University, Norfolk, VA, USA

E. S. Weiser
NASA Langley Research Center, Hampton, VA, USA

Pascal Hubert
Old Dominion University, Norfolk, VA, USA

Abstract

High temperature polymeric foams have been developed from polyimides by three distinct approaches: foaming directly from the powder precursor and through creation of two intermediary precursor mesostructures: friable balloons and microspheres. The present paper focuses on developing an understanding of microsphere and balloon kinematics during formation and growth. The influence of polymer particle size upon balloon and microsphere final dimensions is studied. Several examples of the growth kinetics of polyimide mesostructures are described including the spherical microsphere, the multi-sphere, and the balloon consisting of multiple spherical segments containing rib like structures.

Keywords: Polyimides, Balloons, Powder, Microspheres, Foams.

1. Introduction to Polyimide Foams

The foam precursor was synthesized by mixing monomer reactant oxydiphthalic anhydride (ODPA) with a hydrogen

bonded foaming agent in methanol (MeOH) at room temperature. After three

hours of mixing at 60⁰ C, this material was converted into ODP-dimethyl ester. It was then mixed with measured amounts of 3,4'-oxydianiline (3,4'-ODA), and stirred for two hours to yield a homogeneous solution. A fine powder of salt-like foaming precursor was isolated from the solution by evaporation of the solvent to produce the polyimide precursor powder. The materials discussed in this paper were produced by Unitika Ltd of Japan [1].

Foams are produced from the polyimide precursor powder by a simple thermal cycle under ambient pressure conditions [2]. While the mechanisms for the inflation of the present material have not been studied in detail until the present paper, it is clear that the blowing agent is hydrogen bonded to the precursor particles and upon an increase in temperature, is released while the polymer passes through its glass transition temperature and the particle is transformed into a hollow mesostructure. When, in a confined volume, the microspheres then grow together to produce the foam microstructure.

Three different approaches to produce foams from the polyimide particles containing the blowing agent have been developed in which the three precursor

systems are polymer powder particle, the partially inflated particle with incomplete polymerization and the fully inflated particle with fully developed molecular weight. When the foam is produced directly from the polymer powder, the foaming agent contained in each particle acts to foam the polymer particle and there intersecting growth patterns form the foam. For the partially inflated precursor, the polymer particles are inflated individually without interaction with other particles and taken to a stage short of complete polymerization. They are then closely packed together and subjected to the final foaming process through a thermal cycle. The third precursor form is developed by inflating the polymer particles and achieving the final molecular weight of the polyimide directly and then subjecting the closely packed assembly to a thermal cycle to fuse the microstructure together. Several different mesostructures are formed during these processes and they will be discussed later.

2. Geometric Relationships for Incompressible Polymer

The geometry of polymeric particle can idealized as a hollow microsphere of initial outer radius, b_0 and initial inner radius, a_0 . Under the condition of constant volume of polymeric material, geometric relations can be developed that relate the microsphere radii, b and a , as a function of its initial dimensions.

$$\frac{b}{b_0} = \frac{[1 - (a_0/b_0)^3]}{[1 - (a/b)^3]} \quad (1)$$

$$\frac{a}{b_0} = \left(\frac{a}{b}\right)\left(\frac{b}{b_0}\right) = \left(\frac{a}{b}\right) \frac{[1 - (a_0/b_0)^3]}{[1 - (a/b)^3]} \quad (2)$$

Microsphere size as a function of a/b at $a_0/b_0=0.1$

Equations 1 and 2 give the ratio of the new outer radius to the initial outer radius, b/b_0 and the ratio of the new inner radius to the initial outer radius, a/b_0 as a function of

the initial dimensions of the microsphere and reveal cubic relationships with the ratios of inner to outer diameter. These results are summarized in Fig. 1 for an initial radius ratio of 0.1. Of particular note is the rate of growth of the new outer diameter, b as a function of the inner radius growth. Note, for example that an increase in the size of the inner radius ratio, a/b_0 from 0.1 to 0.427 corresponds to an increase in outer radius ratio, b/b_0 of only 1.0 to 1.067. Therefore, a change in inner radius of over 400% produces only a 7% change in external radius ratio.

Wall thickness as a function of a/b and a_0/b_0

The microsphere wall thickness, t can be expressed as a function of the initial and final radius ratios as shown in Equation 3 and Fig. 2.

$$\frac{t}{b_0} = \frac{[1 - (a_0/b_0)^3]}{[1 - (a/b)^3]} \left[1 - \left(\frac{a}{b}\right) \right] \quad (3)$$

From Fig. 2 it is also clear that the thickness ratio, t/b approaches a limit of approximately 0.33 as a/b_0 approach unity. As will be shown later, this limit is a function of the initial radius ratio of the microsphere.

3. Microsphere growth observations

In order to evaluate the polyimide microsphere behavior when subjected to an increase in temperature from 27.5°C to 190°C the following measurements were undertaken.

Particle size distribution

In an attempt to determine the relationship between polymer particle size and microsphere size, size particle distribution within a typical polymer powder was measured by physical screening. Results presented in Table 1 show that almost 90% of the polymer powder particles

ranged in size from 75 to 500 microns. These results show that the largest dimension of two-thirds of the particles falls in the range of 106-300 microns.

Particle size range, microns	Weight percent
0-75	11.6
75-106	17.2
106-180	28.1
180-300	39.4
300-500	03.5

Table 1: *Particle size distribution.*

Microsphere growth observations

It is instructive to first examine the growth kinetics of a single 203 micron microsphere grown from a 123 micron polymer particle in reverse time because the geometric formation of the microsphere from the single particle is quite complex. Here we can begin with the microsphere in its fully inflated state and measure its outer diameter, wall thickness and inner diameter. As seen in the photographic images shown in Fig. 3-6.

As time is observed in reverse from 16.26 minutes to 12.25 minutes, the diameter of the microsphere is seen to diminish from 202 microns to 103 microns, a reduction of approximately 50%. The wall thickness increases during this interval from 6.4 microns to 19.1 microns. The volume of the polymer within the microsphere appears to range from 2.10 to $3.20 \times 10^{-12} \text{ m}^3$, with an average volume of $2.87 \times 10^{-12} \text{ m}^3$. This volume for an incompressible polymer would correspond to a solid particle initial radius of 88.2 microns or a diameter of 176 microns. For $a_0/b_0 = 0.5$, the hollow microsphere would have a diameter of 349 microns. Clearly, these measurements fall in the range reported above in Table 5.

Microsphere formation

Continuing to observe the microsphere formation in reverse time, it is instructive to examine the polymer particle as it transitions from microsphere to its irregular shape. Fig. 7-9 illustrate this phenomenon. Note that at time of 12.25 minutes (150°C), the particle has assumed a quasi-spherical shape, while at 11.75 minutes (145°C), the particle shape has become irregular. Indeed, as time is observed in reverse, from 11.75 minutes to 0, the particle appears to grow in planar dimensions. The approximate planar area of the particle grows from 7.3 to $11.3 \times 10^{-9} \text{ m}^2$ as time is viewed from 11.75 to 0 minutes. In other words, the particle planar dimensions are seen to decrease with increasing time and temperature.

In the second matrix of data, estimates of the particle volume are made. Here the average lateral dimension of the particle is multiplied by 0.3 in order to estimate the thickness dimension of the particle. Next the plan form area of the particle is multiplied by the estimated thickness in order to estimate the particle volume. The particle volume estimates ranged from 2.65 to $4.14 \times 10^{-13} \text{ m}^3$. In contrast to the volume estimate of $2.87 \times 10^{-12} \text{ m}^3$ taken from the microsphere geometries, the average particle volume estimate is only $3.36 \times 10^{-13} \text{ m}^3$ or a factor of 8.5 difference – almost an order of magnitude difference. Clearly the simplifying assumption of constant volume throughout the process is not exact.

The experimental data are compared to the geometric predictions in Fig. 10 and 11. Here the initial radius ratio of 0.85 was chosen after comparing the experimental data to Equation 1 and arriving at an average value over the range 0.923-0.772. These figures show that the geometric relations for b/b_0 , a/b_0 and t/b_0 are not in close agreement with the experimental results. Indeed, the results confirm that for the microsphere observed, the constant volume approximation is not a good one, even over the range in geometries wherein

the microsphere has taken form. Clearly the observed deformations of the irregular shaped particle differ quite substantially from that of a constant volume, incompressible solid as well.

Influence of particle size on mesostructure formation

The influence of particle size upon the final dimensions of the mesostructure formed can be assessed by studying the particles of five distinct average dimensions: 50.4, 76.7, 86.7, 190 and 280 (microns). As shown in Table 2, the corresponding microsphere diameters were found to be 78, 71, 173, 382 and 658 microns. If the particles are taken to be solid microspheres with the dimensions of the average particle size, the volume of polymer available for inflation and be calculated and estimates of final wall thickness determined as shown in Table 2.

Avg. Particle Dim (μm)	Micro-sphere Radius (μm)	$(3/4\pi)$ Vol. $\times 10^{-14}$	Est. Wall thick. (μm)
50.4	38.8	1.60	4.0
76.7	35.5	5.66	NA
86.7	86.5	8.18	3.8
190.0	191.0	85.7	13.2
280.0	329.0	274.4	8.7

Table 2: *Particle size effects.*

Mesostructure forms

There were three different mesostructures observed in the foaming of individual polymer particles. The first is the simple hollow microsphere with wall thickness only a few percent of the microsphere outer radius. The second mesostructure consists of two or more intersecting microspheres and the third mesostructure consists of a rib-like structure that bounds spherical segments. These three

characteristic mesostructures are illustrated in Fig. 12.

Influence of particle size on mesostructure

The influence of particle size on mesostructure is best achieved by observing the inflation kinetics of polymer particles that differ only in size: 75, 106, 180 and 300 microns. In Fig. 13 and 14 the 75 and 106 micron particles are seen to inflate into a mesostructure of a single microsphere. In contrast the 180 and 300 micron particles shown in Fig. 15 and 16 develop a rib like structure with multiple spherical segments as discussed earlier. In addition, the 300 micron particle results presented in Fig. 16 show that the larger particle contains enough polymeric volume to fill large amounts of space and thereby develop the desired foam structure.

4. Results and discussion

The results of this preliminary study provide an insight into the inflation kinetics of a polyimide foam wherein the polyimide particle contained trapped blowing agent and an increase in temperature resulted in the inflation of individual polyimide particles. A constant volume geometric analysis showed that the polymer volume available for the creation of microspheres is limited by the particle size, but that the volume of the hollow spherical particle may differ only slightly from the solid particle if the ratio of inner to outer radius does not exceed 0.4. It was also observed that the wall thickness of a microsphere of a polymer of constant volume approaches a value of approximately 0.3 times the equivalent solid particle radius. Thus, one can estimate the wall thickness of microspheres with ratio of inner to outer radii greater than 0.9 by this simple rule.

The particle size distribution was measured and almost two-thirds of the particles were found to fall between 106-

300 microns. The average observed volume in the microsphere phase was shown to correspond to a solid spherical particle of diameter equal to 176 microns.

Experimental data were presented for the inflation of a single polyimide particle containing blowing agent by raising the temperature at a rate of 10^0 C/min. from 27.5 to 190⁰ C. By observing photographic images taken at known time and temperature intervals, the inflation kinetics could be separated into two phases. The first phase was found to be simple dimensional changes of a hollow microsphere with approximately constant polymer volume. The second phase was the transformation of the particle from an irregular shape to a microsphere. In this phase, the particle appeared to shrink as time and temperature were increased. Indeed, the estimated volume of the irregular polymer precursor particle appeared to be an order of magnitude less than that of the final microsphere.

The assumption of conservation of volume throughout the particle transformation and inflation processes has been shown to be a poor approximation and the need for a more rigorous treatment of this process is clearly evident.

Three distinct polymeric mesostructures were described and illustrated: single sphere, multiple intersecting spheres and the rib and spherical element structures. Inflation kinetics was observed for polymer particles ranging in size from 75 to 300 microns and the mesostructure developed was shown to be a function of particle size. The most desirable mesostructure wherein the maximum space was filled with the rib like structure was developed by particles of 180 microns and greater.

5. References

- [1] Hou, T.H., Weiser, E.S., Siochi, E.J. and St Clair, T.L., Proceedings of

SAMPE Annual Conference, 1999, pp 1792-1807.

- [2] Pipes, R.B., Weiser, E.S., Gonsoulin, B. and Hubert, P., Proceedings of SAMPE Annual Conference, 2002.

6. Nomenclature

a_0 = initial inner radius
 b_0 = initial outer radius
 a = inner radius
 b = outer radius
 t = wall thickness

7. Figures

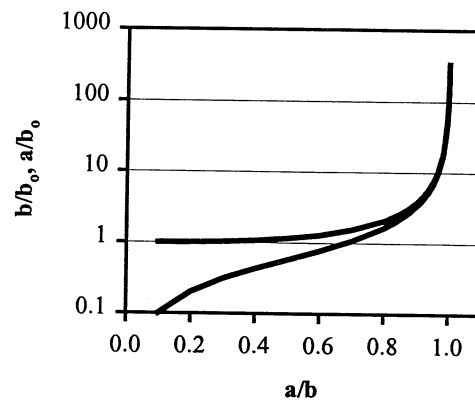


Figure 1: *Microsphere size as a function of a/b at $a_0/b_0=0.1$.*

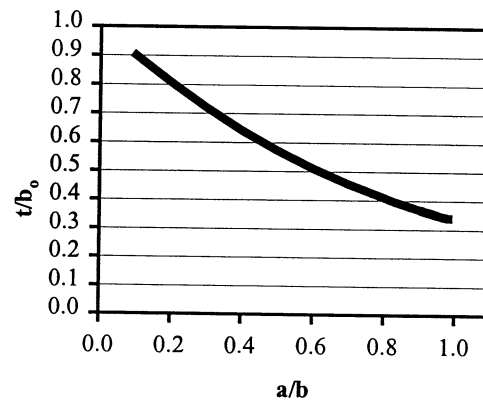


Figure 2: *Microsphere wall thickness as a function of a/b at $a_0/b_0=0.1$.*

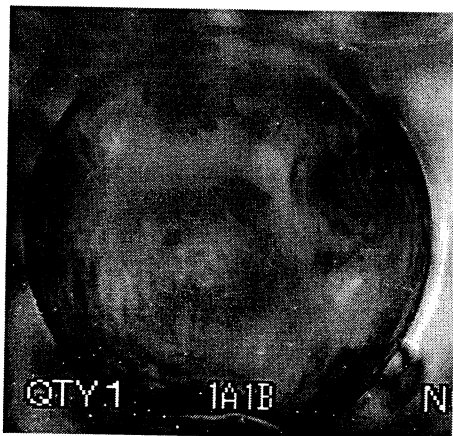


Figure 3: *Polyimide microsphere at 190°C.*

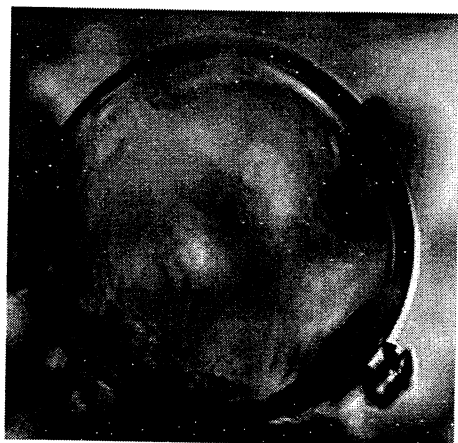


Figure 4: *Polyimide microsphere at 155°C.*



Figure 5: *Polyimide microsphere at 151°C.*

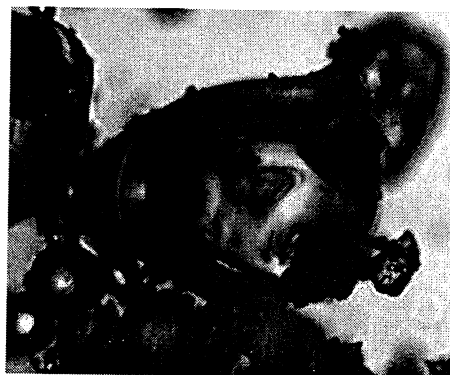


Figure 6: *Polyimide particle at 150°C.*



Figure 7: *Polyimide Particle at 145°C.*



Figure 8: *Polyimide particle at 138°C.*



Figure 9: *Polyimide particle at 27.5°C.*

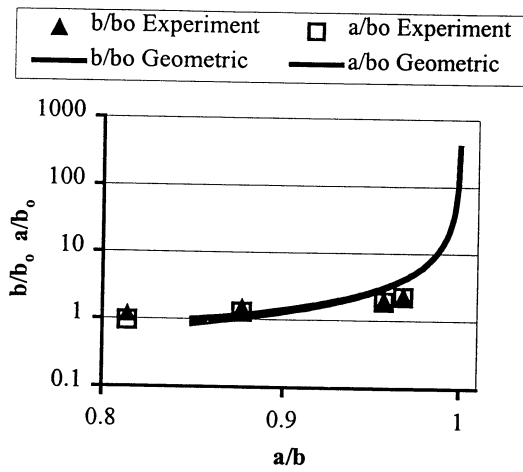


Figure 10: Experimental results for microsphere size as a function of a/b at $a_0/b_0=0.85$.

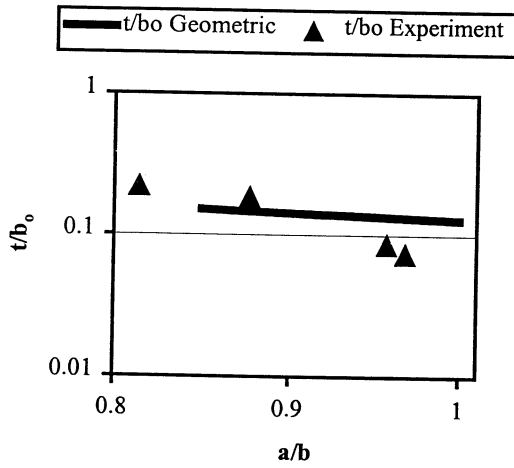
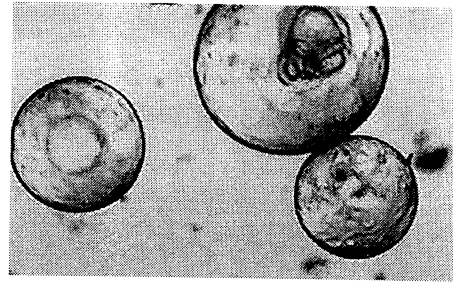
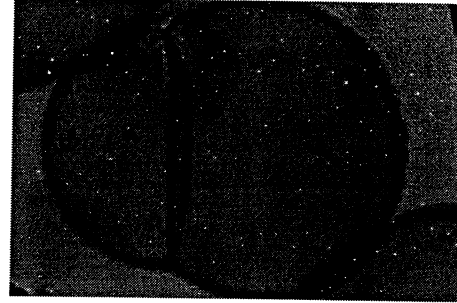


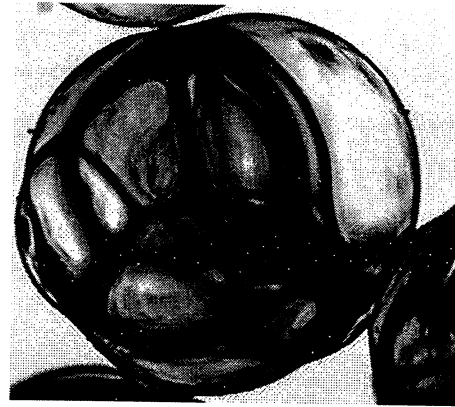
Figure 11: Experimental results for microsphere wall thickness as a function of a/b at $a_0/b_0=0.85$.



a)



b)



c)

Figure 12: a) Simple sphere mesostructure, b) Multisphere mesostructure, c) Rib and spherical segments mesostructure.

Figure 14: 106 micron particle at 200°C.

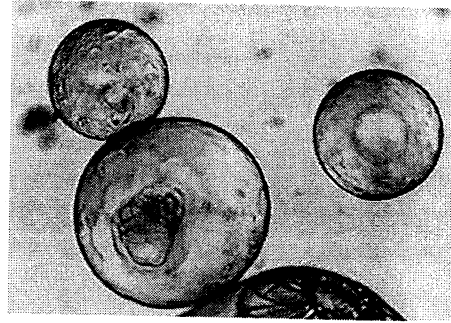


Figure 13: 75 micron particle at temperatures from 23.9-182°C.

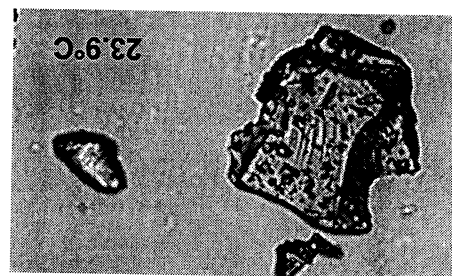
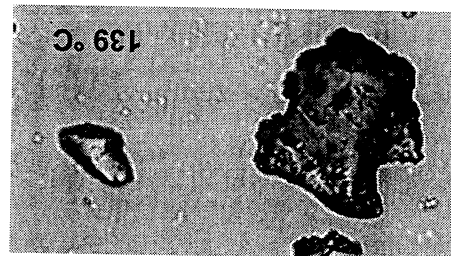
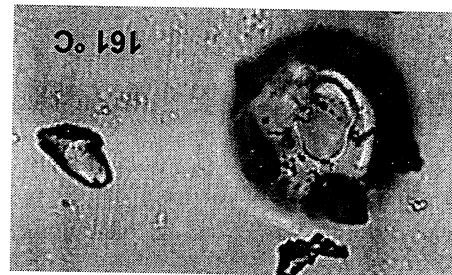
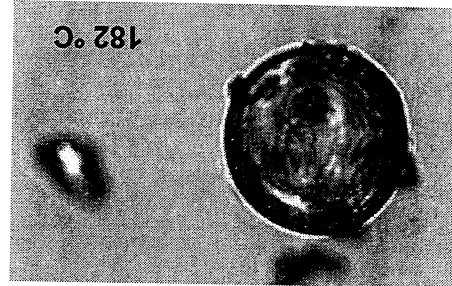


Figure 16: 300 micron particle at temperatures from 18.5-150°C.

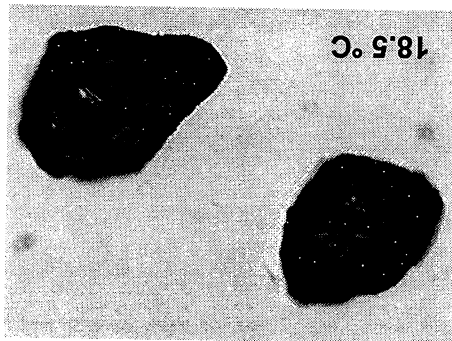
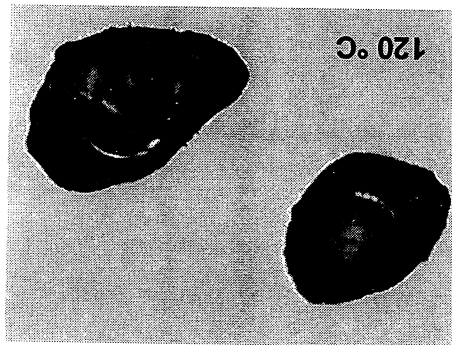
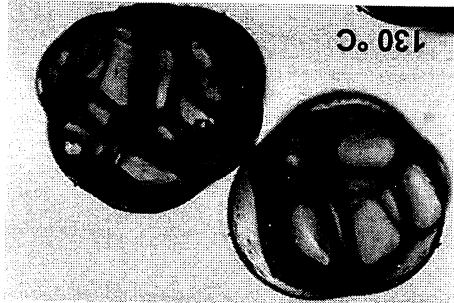


Figure 15: 180 micron particle at 145°C.

